RSC Advances

ROYAL SOCIETY OF CHEMISTRY

PAPER

View Article Online
View Journal | View Issue

Cite this: *RSC Adv.*, 2026, **16**, 12934

Spectroscopic insights into the antibacterial and antifungal mechanism of ZnO nanoparticles green-synthesized from *Morinda citrifolia* leaf extract

Tien Cam Thi Nguyen,[ab] Phuc My Thi Truong,[abc] Ly Ngoc Thi Le,[abc] Uyen Tu Thi Doan,[ab] Khanh Duy Nguyen,[bd] Ngoc Kim Pham,[bc] Vinh Cao Tran,[abe] Lan My Thi Nguyen*[bf] and Anh Tuan Thanh Pham*[ab]

This study presents a green hydrothermal synthesis process for ZnO nanoparticles using *Morinda citrifolia* leaf extract at pH conditions (2.5, 5.0, 7.5, and 10.0). The phytochemical constituents of the extract, including alkaloids, flavonoids, phenolics, coumarins, terpenoids, anthocyanins, and glycosides, served as effective reducing and stabilizing agents. Structural and morphological characterization *via* SEM, XRD, and FTIR confirmed the formation of the hexagonal wurtzite phase (JCPDS 36-1451), consisting of nearly spherical nanoparticles that form dense, agglomerated clusters of ZnO nanoparticles with an average crystallite size of ~12.61 nm. Importantly, Raman and PL spectra provided insight into the antibacterial and antifungal mechanism, revealing that ZnO nanoparticles synthesized at pH 5.0 had a high concentration of oxygen vacancies (V_O), with visible emission accounting for approximately 80% of the total spectrum. This high defect density correlated with superior antimicrobial efficacy. At a concentration of 0.1 mg mL^{-1}, ZnO nanoparticles exhibited significant inhibition zones against *Staphylococcus aureus* (17.05 ± 0.25 mm), *Escherichia coli* (17.62 ± 0.72 mm), and *Candida albicans* (13.39 ± 1.01 mm). These findings demonstrate the potential of ZnO nanoparticles mediated by *Morinda citrifolia* as potent antimicrobial agents and highlight the role of surface defects in enhancing their bioactivity.

Received 24th January 2026
Accepted 24th February 2026

DOI: 10.1039/d6ra00644b

rsc.li/rsc-advances

1. Introduction

Antibiotic resistance has emerged as a critical global health challenge due to the prolonged and excessive use of conventional antibiotics.[1] This crisis has necessitated the development of alternative antimicrobial strategies, among which metal oxide nanomaterials have attracted significant attention.[2,3] Zinc oxide nanoparticles (ZnO NPs), in particular, demonstrated strong antimicrobial activity through multiple mechanisms,[4] including reactive oxygen species (ROS) generation,[5] Zn^{2+} ion release,[6] and membrane disruption,[7] all of which contributed to oxidative stress and microbial cell death.[8–10] These mechanisms are intrinsically linked to the surface properties and crystal defects of the nanoparticles, which can be probed *via* spectroscopic techniques. While various chemical and physical methods exist for ZnO NP synthesis, they often suffer from high energy consumption and the use of toxic reagents, limiting their biocompatibility and sustainability. Consequently, green synthesis utilizing biological templates has gained prominence as an eco-friendly and scalable alternative.[11–14] Its suitability stems from its lower energy consumption, minimal use of toxic chemicals, biodegradability, and potential for large-scale production.[15] Recent studies have further underscored the versatility of oxide-based nanobiocomposites, such as g-C_3N_4 and starch-capped nanostructures, for high-sensitivity sensing and pharmaceutical applications.[16,17] These advancements highlight that the functional performance of oxide nanomaterials is intrinsically governed by their surface states and structural integration. Moreover, the development of magnetized antibacterial nanobiocomposites from biological waste has demonstrated the potential for scalable wastewater disinfection and environmental remediation.[18]

Among them, plant-mediated synthesis emerged as the most practical and scalable alternative due to its simplicity, cost-effectiveness, rapid reaction rates, and ability to yield nanoparticles with diverse morphologies and enhanced stability.[13,14]

[a]*Laboratory of Advanced Materials, University of Science, Ho Chi Minh City, Vietnam. E-mail: pttanh@hcmus.edu.vn*

[b]*Vietnam National University, Ho Chi Minh City, Vietnam. E-mail: ntmlan@hcmus.edu.vn*

[c]*Faculty of Materials Science and Technology, University of Science, Ho Chi Minh City, Vietnam*

[d]*Faculty of Physics and Engineering Physics, University of Science, Ho Chi Minh City, Vietnam*

[e]*Advanced Materials Technology Institute, Vietnam National University, Ho Chi Minh City, Vietnam*

[f]*Faculty of Biology and Biotechnology, University of Science, Ho Chi Minh City, Vietnam*

Morinda citrifolia, commonly known as noni, is a tropical plant native to Southeast Asia that presents an ideal candidate for nanoparticle biosynthesis. Unlike its extensive ethnomedicinal history, the current interest lies in its rich phytochemical profile relevant to nanotechnology. *Morinda citrifolia* leaves contain a high concentration of bioactive compounds, including phenols, flavonoids, alkaloids, and glycosides. These specific phytochemicals possess abundant hydroxyl and carboxyl groups that function effectively as dual-action agents: reducing metal precursors and stabilizing the resulting nanoparticles to prevent agglomeration.[19] By leveraging these natural reducing agents, the synthesis process becomes not only safer but also more controlled.

In this study, we report the green hydrothermal synthesis of ZnO NPs using *Morinda citrifolia* leaf extract. The novelty of this work lies in providing deep spectroscopic insights into the antimicrobial mechanism by establishing a quantitative link between pH-modulated structural defects and biological outcomes. Unlike previous studies that focus primarily on synthesis routes, this research utilizes quantitative PL deconvolution to identify specific defect states, particularly singly ionized oxygen vacancies (V_O^+) and correlates them with antibacterial (against *S. aureus* and *E. coli*) and antifungal (against *C. albicans*) performance. By integrating Raman and Photoluminescence (PL) spectroscopy, we elucidate how the synthesis pH transitions defects from surface-active V_O^+ (at pH 5.0) to deeper, less bioactive V_O^{2+} and O_i states (at pH 10.0). This approach provides a rigorous physicochemical framework to explain why high antimicrobial efficacy can be maintained even when particle aggregation occurs, thereby advancing the field of defect-engineered biogenic nanomaterials.

2. Experimental

2.1. Preparation of *Morinda citrifolia* leaf extract

Morinda citrifolia, a plant in the Rubiaceae family, was obtained from a garden in Kien Giang, Vietnam. To eliminate dust and contaminants, the leaves were properly washed multiple times with tap and deionized water before being dried at 100 °C for 12 hours. The dried leaves were finely ground into a powder and preserved. For the extraction, 2 g of leaf powder was mixed with 100 mL of ethanol and stirred magnetically at 25 °C for 2 hours. Following filtering, the *Morinda citrifolia* extract (MCE) was collected and stored at 4 °C for further study. The natural compounds in MCE were tested as shown in Table 1.

2.2. Synthesis of ZnO NPs

Zinc nitrate hexahydrate ($Zn(NO_3)_2 \cdot 6H_2O$, 98%, Thermo Scientific), sodium hydroxide (NaOH, 99.8%, Sigma-Aldrich), and ammonia solution (NH_4OH 35%, Merck) were utilized to control the pH.

The synthesis route of ZnO NPs is illustrated in Fig. 1. Initially, the reduction of $Zn(NO_3)_2$ was achieved by combining 80 mL of *Morinda citrifolia* extract (MCE) with 2.38 g of $Zn(NO_3)_2 \cdot 6H_2O$ and then stirring for 2 hours to ensure complete dissolution of zinc nitrate. Adjust the pH of the mixture to the values of 2.5, 5.0, 7.5, and 10.0. The mixture has undergone a hydrothermal process in an autoclave at 120 °C for 8 hours. After cooling to room temperature, the product is centrifuged at 9500 rpm for 3 minutes and washed with ethanol. The resulting precipitate is then calcined at 400 °C for 4 hours to obtain ZnO NPs.

2.3. Characterization of ZnO NPs

Surface morphology and particle size of ZnO NPs were analyzed using a scanning electron microscope (SEM, Jeol JSM-IT200). This technique was employed to examine the surface features, shape, and approximate size distribution of the nanoparticles. The determination of the crystalline size and structural properties of ZnO NPs was studied using a Bruker D8-Advanced X-ray diffractometer (XRD) with CuKα radiation. The mean crystalline size (D) was calculated using the Scherrer equation: $D = 0.9\lambda/\beta \cos\theta$, where λ is the X-ray wavelength, β is the full width at half maximum, and θ is the diffraction angle. To identify the functional groups responsible for the capping and stabilization of the nanoparticles, Fourier Transform Infrared (FTIR) spectroscopy was performed using a TENSOR 27 Bruker spectrometer in the wavenumber range of 400–4000 cm^{-1}. Raman spectroscopy was conducted using a Horiba XploRa+ microscope equipped with a 532 nm excitation laser to investigate the vibrational modes and structural properties of ZnO NPs. Photoluminescence (PL) spectroscopy was performed using a fluorescence spectrometer (Horiba iHR550) with an excitation wavelength of 355 nm to evaluate the optical properties and defect states in the ZnO NPs. The emission spectra were recorded in the range of 360–750 nm with appropriate slit widths and

Table 1 Qualitative test for natural compounds

	Natural compounds	Test	Test reagent	Positive test
1	Akaloids	Wagner's test	Wagner's reagent	Reddish-brown precipitate[9]
2	Phenolics	Ferric chloride test	5% ferric chloride sol	Dark green colouration[9]
3	Anthocyanin	HCl test	2 N sodium hydroxide and heated for 5 min at 100 °C	Bluish green colour[10]
4	Flavonoids	Alkaline reagent test	10% ammonium hydroxide sol	Yellow fluorescence[9]
5	Terpenoids	Salkowski test	MCE extracted from chloroform + H_2SO_4	Yellow-green fluorescence at the interface[20]
6	Coumarins	NaOH test	NaOH 10%	Yellow colouration[21]
7	Glycosides	Keller–Killani test	$FeCl_3$ 5% + H_2SO_4	Reddish-brown ring at the interface[20]

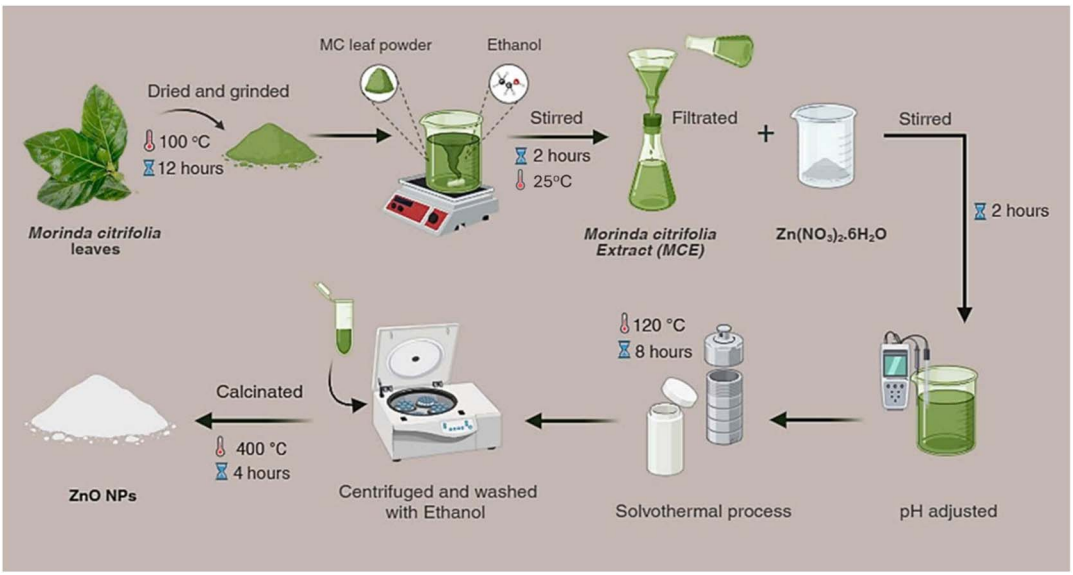

Fig. 1 Preparation scheme of ZnO NPs from *Morinda citrifolia* leaves.

integration time to ensure an optimal signal-to-noise ratio. To quantify the relative concentration of specific defects, the broad emission bands were mathematically deconvoluted into individual sub-peaks using Gaussian fitting functions. The relative contribution of each emission component was then calculated as the ratio of its integrated area to the total area of the PL spectrum. Finally, the surface charge and colloidal stability of the synthesized nanoparticles were evaluated by measuring the zeta potential using a Horiba SZ-100 at neutral pH and room temperature.

2.4. Minimum inhibitory concentration, minimum bactericidal concentrations

The Minimum Inhibitory Concentration (MIC) is the lowest concentration of a chemical that prevents bacterial growth. Resazurin (7-hydroxy-3*H*-phenoxazine-3-one-10-oxide) is a colorimetric indicator that is sensitive to the bacterial dehydrogenase enzyme. Living cells convert resazurin (blue, non-fluorescent) to resorufin (pink, fluorescent), which indicates bacterial viability. Conversely, the absence of metabolic activity due to bacterial inhibition or death is indicated by the solution remaining blue.

Each test Eppendorf included 100 μL of ZnO NPs solution (at concentrations of 0.5, 1.0, 1.5, 2.0, and 2.5 mg mL^{-1}), combined with 800 μL of Mueller–Hinton broth (MHB) and 100 μL of bacterial suspension at a cell density of 10^6 CFU mL^{-1}. Streptomycin 0.1 mg mL^{-1} served as the positive control, while 2% DMSO was used as the negative control. Following 24 hours of incubation at 37 °C, 10 μL of resazurin 0.5 mg mL^{-1} was added to each microwell. After an additional incubation period of 30 minutes at 37 °C, the MIC was determined as the lowest concentration that remained blue, indicating bacterial suppression. The Minimum Bactericidal Concentrations (MBC) were determined based on the number of colonies on Mueller–Hinton Agar (MHA) medium Petri dishes at the MIC concentration after 24 h of incubation at 37 °C. According to the formula:

$$\%\ \text{Bactericidal ratio} = \left(1 - \frac{Z}{C}\right) \times 100$$

where Z and C (CFU mL^{-1}) represent the colony-forming units per milliliter in the test sample containing ZnO NPs and the control sample. The bactericidal activities were evaluated by measuring the survival rate of microorganisms after exposure to ZnO NPs in the test sample, compared to the control sample without ZnO NPs.

2.5. Antibacterial and antifungal susceptibility testing

The antibacterial and antifungal activities of ZnO NPs were assessed against three different pathogenic strains: Gram-positive (*S. aureus*), Gram-negative (*E. coli*), and *C. albicans*. All microbial strains were obtained from the Laboratory of Plant Biotechnology and Biomodification, Faculty of Biology and Biotechnology, University of Science, Vietnam National University Ho Chi Minh City, Vietnam.

The antibacterial and antifungal activity of 100 μL ZnO NPs 0.10 mg mL^{-1} was determined using the agar well diffusion assay. The inhibitors diffused through the agar and inhibited bacterial growth. *E. coli*, *S. aureus*, and *C. albicans* were cultured in MHB diluted to a cell density of 10^6 CFU mL^{-1} and spread evenly on the surface of MHA Petri plates. The wells were formed with a diameter of 6 mm. ZnO NPs were loaded into the wells. The plates were incubated at 37 °C for 24 h, and the diameters of the inhibition zones were measured.

Each experiment was repeated three times, data are presented as mean ± SE ($n = 3$), and statistically significant differences were tested with $P < 0.05$. Data analysis was performed using Microsoft 365 Excel statistical software using the one-way ANOVA method.

3. Results and discussion

3.1. Natural compounds *Morinda citrifolia* leaves

To identify the bioactive agents responsible for the reduction and stabilization of ZnO NPs, both qualitative phytochemical screening and FTIR spectral analysis were conducted. As shown in Fig. 2, the qualitative screening of the *Morinda citrifolia* leaf extract confirmed the presence of alkaloids, phenolics, flavonoids, terpenoids, coumarins, and glycosides. These findings are consistent with those reported by Shoge and co-workers.[22] To structurally corroborate these qualitative findings, the FTIR spectrum of the extract was analyzed (Fig. 2). The spectrum exhibits a broad, intense absorption band at 3358 cm^{-1}, attributed to the O–H stretching vibrations of the hydroxyl groups present in the phenolics and flavonoids identified in the qualitative screening.[23] The peaks at 2922 cm^{-1} and 2852 cm^{-1} correspond to the C–H stretching of aliphatic chains, likely associated with terpenoids or lipids.[24] Furthermore, the peak at 1741 cm^{-1} (C=O stretching) and 1639 cm^{-1} (C=C aromatic stretching or amide I) confirm the presence of carbonyl groups and aromatic rings,[25] which are characteristic of flavonoid frameworks and protein residues. The strong band at 1049 cm^{-1} (C–O stretching) aligns with the presence of glycosides.[26] The combined qualitative and FTIR data conclusively demonstrate that the *Morinda citrifolia* extract is rich in multifunctional biomolecules. These compounds serve a dual purpose: the phenolics and flavonoids act as reducing agents ($Zn^{2+} \rightarrow Zn^{0}$), while the terpenoids and proteins function as capping agents, providing steric stability to the synthesized ZnO nanoparticles. MCLE easily and rapidly reduced and dispersed nanoparticles well. Many biomolecules in plants could participate in the bioreduction, formation, and stabilization of ZnO NPs. The reducing ability of ions and the reducing ability of plants depend on the presence of polyphenols, enzymes, and other complexing agents present in plants, which have an important impact on the amount of nanoparticle production.[16]

3.2. Morphological analysis

ZnO NPs synthesized at pH = 2.5 and pH = 5.0 (Fig. 3a and b) exhibit nearly spherical nanoparticles forming dense, agglomerated clusters with an average particle size of 77.1 ± 12.2 nm and 81.8 ± 12.2 nm, respectively, with noticeable agglomeration forming nanoparticle clusters. The strongly acidic environment (pH 2.5) can partially dissolve ZnO *via* the reaction, $ZnO + 2H^{+} \rightarrow Zn^{2+} + H_2O$, leading to the rapid formation of Zn^{2+} ions and accelerating the saturation rate of Zn^{2+} ions. This phenomenon results in the uncontrolled aggregation of nanoparticles, predominantly around 80 nm, contributing to a moderate polydispersity with a relative standard deviation (RSD) of 15.75%. As the pH increases to 5.0, ZnO NPs exhibit reduced aggregation, with particle sizes ranging from approximately 70 to 90 nm, creating more favorable conditions for crystallization and improving particle homogeneity, as evidenced by a narrower RSD of 14.86%.

At pH = 7.5 (Fig. 3c), further improvements in morphology and size distribution are observed, with an average particle size of 84.0 ± 12.8 nm, mainly within the 60–102 nm range. The neutral pH condition suppresses excessive aggregation and enhances ZnO NPs' uniformity, maintaining an RSD of 15.22%. The high-density distribution of nanoparticle clusters without significant voids or large gaps indicates that, under this condition, a well-balanced nucleation and growth process is maintained, limiting aggregation and contributing to a homogeneous structure. Compared with previous studies, Senthilkumar *et al.* synthesized ZnO NPs using a biological method with *Tectona grandis* leaf extract and also observed uniform nanoparticle distribution under neutral pH conditions.[27]

At pH = 10 (Fig. 3d), a significant increase in particle size and pronounced aggregation are observed. The nanoparticles are tightly bound, forming larger clusters, which reduces dispersion uniformity. The average particle size reaches 159.5 ± 38.3 nm. This phenomenon is primarily attributed to the formation of $[Zn(NH_3)_4]^{2+}$ complexes in a strongly alkaline medium:

$$Zn^{2+} + NH_3 \rightleftharpoons [Zn(NH_3)]^{2+}$$

$$[Zn(NH_3)]^{2+} + 3NH_3 \rightleftharpoons [Zn(NH_3)_4]^{2+}$$

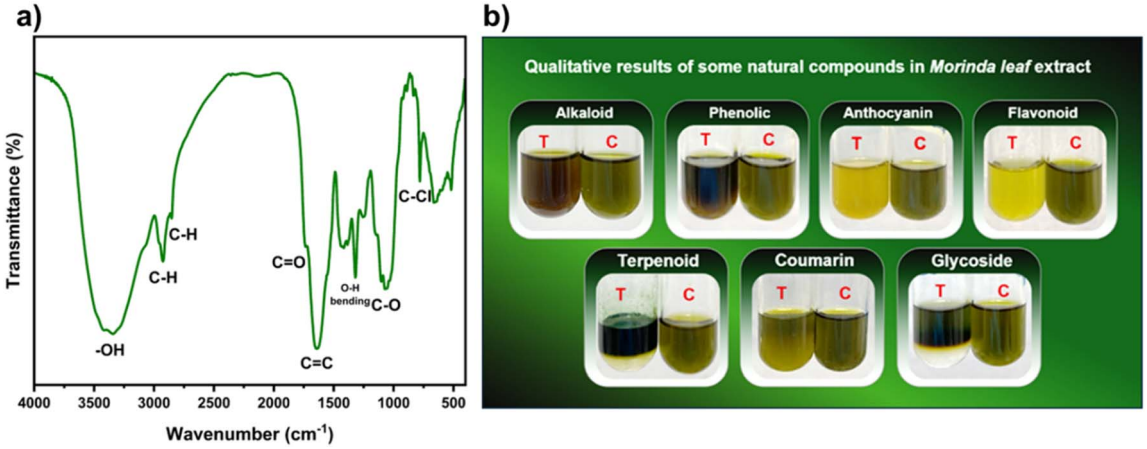

Fig. 2 (a) FTIR (b) qualitative results of some natural compounds in *Morinda citrifolia* leaves extract.

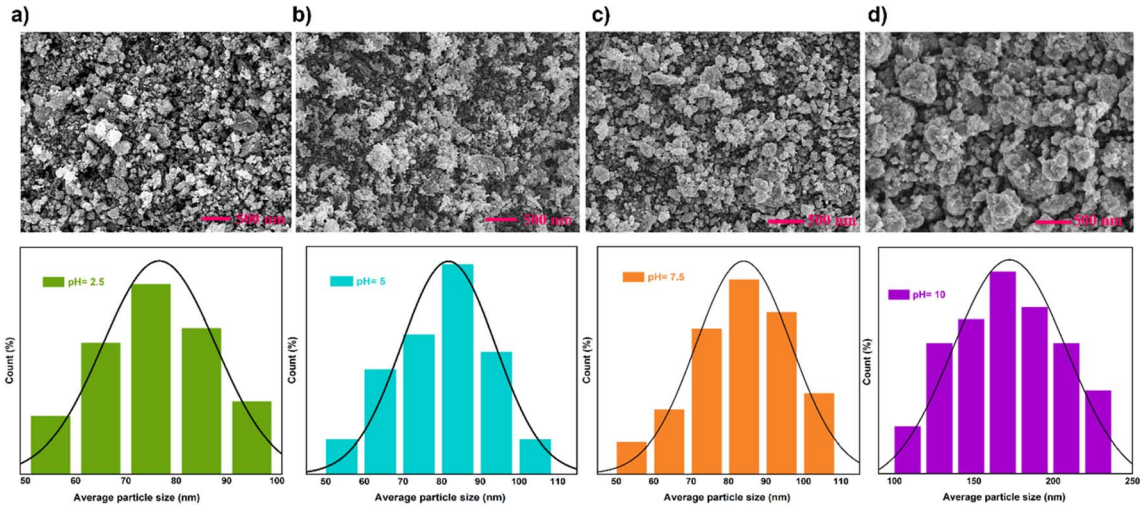

Fig. 3 SEM images and particle size distributions of ZnO NPs synthesized at different pH levels: (a) pH = 2.5, (b) pH = 5.0, (c) pH = 7.5, and (d) pH = 10.

Simultaneously, the high OH^- ion concentration in the alkaline environment promotes $Zn(OH)_2$ formation *via* the reaction:

$$Zn^{2+} + 2OH^- \rightarrow Zn(OH)_2\downarrow$$

However, $Zn(OH)_2$ is an amphoteric hydroxide that can dissolve in a strongly alkaline medium to form $Zn(OH)_4^{2-}$ ions:

$$Zn(OH)_2 + 2OH^- \rightarrow [Zn(OH)_4]^{2-}$$

This leads to increased nanoparticle interaction, reducing colloidal stability and increasing particle cluster size.[28] Consequently, the polydispersity increases significantly, with the RSD reaching 23.99%, indicating large size variability. Additionally, this phenomenon may be associated with insufficient thermal treatment to completely remove residual organic impurities. When the pH exceeds the isoelectric point of ZnO, aggregation intensifies, reducing the available surface area and affecting the dispersion stability of ZnO NPs.[29] For example, Abdulrahman *et al.* reported that the morphological variations of ZnO synthesized in NH_4OH media (pH 6.7–12) are associated with the formation of intermediate hydroxyl or ammine species in solution, including $[Zn(NH_3)_4]^{2+}$ and tetrahedral Zn complexes.[30] The presence and stability of these species in alkaline conditions can significantly influence the nucleation and growth behaviors of ZnO.

These observations are consistent with the histogram plots (Fig. 3a–d), which clearly illustrate the influence of pH on particle size uniformity. At pH 2.5, the histogram is broad and slightly asymmetric, with particle sizes mainly in the 70–80 nm range, indicating high polydispersity. At pH 5.0 and 7.5, the distributions are narrower and more symmetric (Gaussian-like), representing the highest degree of size uniformity (RSD < 15.3%). In contrast, the histogram at pH 10.0 becomes substantially broader, quantitatively confirming the large size variability associated with the peak alkaline-induced aggregation. In contrast, the histogram at pH 10 becomes substantially broader (120–200 nm), demonstrating large size variability due to pronounced aggregation.

3.3. FTIR analysis

The biosynthesized ZnO nanoparticles (ZnO NPs) exhibited characteristic absorption peaks in their FTIR spectra, notably at 3413, 1450, 860, and 455 cm^{-1} (Fig. 4). The prominent signal at 3413 cm^{-1} is attributed to the stretching vibration of O–H groups,[31] confirming the presence of phenols and alcohols on the NP surface. The peak at 1450 cm^{-1} can be attributed to C=O stretching of carboxylic acids present in the *Morinda citrifolia* extract.[32] Crucially, the peak located at 455 and 860 cm^{-1} falls within the range attributed to the characteristic Zn–O stretching vibration,[33] confirming the formation of the wurtzite

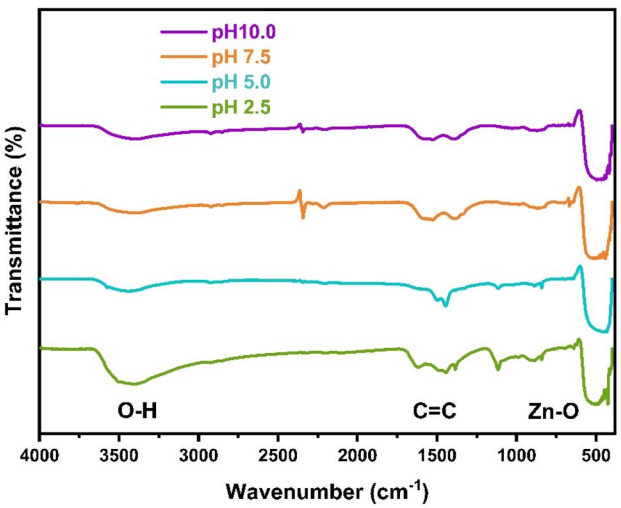

Fig. 4 FTIR spectra of biosynthesized ZnO NPs prepared at different pH values.

crystalline structure. The presence of these organic functional groups on the surface of the ZnO NPs, even after washing, confirms that the phytoconstituents act as effective capping agents, playing a crucial role in preventing agglomeration and stabilizing the nanoparticles.

3.4. Crystalline characteristics

Fig. 5 shows the XRD patterns that confirmed the crystalline phase and crystallinity of ZnO nanoparticles synthesized using *Morinda citrifolia* leaf extract at different pH levels. All the samples displayed distinct Bragg reflection peaks matching the hexagonal wurtzite structure of ZnO (JCPDS 36-1451) with lattice parameters $a = 3.2758$ Å and $c = 5.2435$ Å.[34] The absence of additional peaks confirmed phase purity, indicating that the zinc precursor was fully converted into ZnO without residual impurities. These results affirm that the natural compound in the noni leaf extract effectively facilitated the formation and stabilization of ZnO NPs. They acted as reducing agents and protected the outer surface of the zinc nitrate hexahydrate molecules, thereby promoting ZnO NP formation.

The XRD patterns of the samples synthesized at different pH values show noticeable variations in peak width and intensity, although the trend is non-linear. Nevertheless, the results clearly indicate that pH affects the crystallinity of ZnO. At pH 2.5, the diffraction peaks, particularly the (101) plane, are sharper and more intense, suggesting a relatively well-ordered crystal arrangement under mildly acidic conditions. In contrast, the sample prepared at pH 5.0 exhibits broader peaks with slightly reduced intensity, consistent with a smaller crystallite size and greater peak broadening. At pH 7.5, the peaks become sharper (FWHM = 0.437) and the crystallite size reaches its maximum value (14.88 nm), indicating that near-neutral conditions provide a more favorable balance between nucleation and growth. For the samples synthesized at pH 7.5 and 10, the diffraction peaks remain broadened, and their intensity decreases, suggesting that higher pH values may reduce crystallite coherence or introduce lattice strain. Notably,

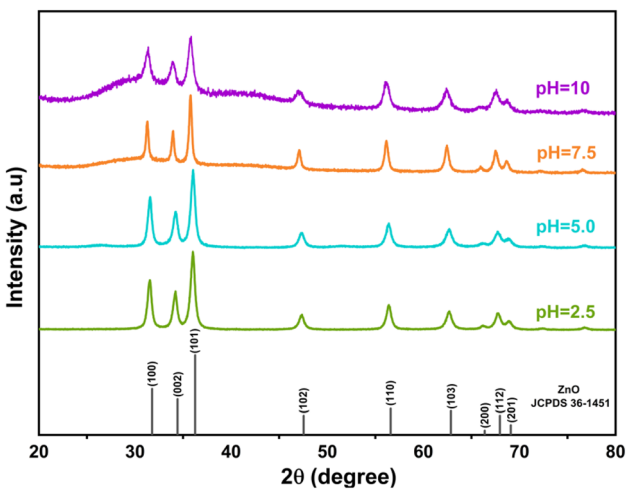

Fig. 5 XRD pattern for *Morinda citrifolia* leaves-mediated ZnO NPs with different pH values.

Table 2 Effect of pH value on crystal size and lattice parameters of ZnO NPs

Sample	FWHM	2 theta (deg.)	Crystallite size (nm)	Lattice parameters
pH = 2.5	0.651	36.005	12.97	$a = 3.2$ Å $c = 5.2$ Å
pH = 5.0	0.649	36.024	12.61	$a = 3.2$ Å $c = 5.2$ Å
pH = 7.5	0.437	35.767	14.88	$a = 3.2$ Å $c = 5.2$ Å
pH = 10	0.712	35.771	10.78	$a = 3.2$ Å $c = 5.2$ Å

the pH 10 sample shows the largest FWHM value (0.712) and the smallest crystallite size (10.78 nm), which may be associated with the formation of Zn-hydroxo/ammine species and increased lattice strain under strongly alkaline conditions.[35]

These trends were consistent with the calculated crystallite sizes, which ranged from 10.78 nm to 14.88 nm and correlated with full-width at half maximum (FWHM) values observed at the main diffraction peaks (Table 2). At low pH, the dominant process is the partial dissolution of ZnO due to proton attack, rather than oxidation. This dissolution competes with crystal growth and results in smaller crystallite domains. At high pH, the formation of hydroxo or ammine of Zn^{2+} complexes and the increase in lattice strain during rapid nucleation introduce structural defects, which can promote particle aggregation. The diffraction peak intensity also decreases at higher pH, particularly at pH 10, consistent with defect formation and reduced crystallinity. This reduction in intensity and peak broadening at higher pH values suggested the presence of crystal defects or irregular crystallization processes.[35,36] Anyway, all the samples retained the hexagonal ZnO structure.

The multi-crystalline structures within each particle were a feature that increased the number of surface-active sites and enhanced the generation of ROS, which play a key role in damaging bacterial membranes, proteins, and DNA. Additionally, the pH of the synthesis environment influenced the release of Zn^{2+} ions from ZnO NPs. At lower pH values (2.5–5), ZnO dissolution to Zn^{2+} occurred more readily, facilitating antimicrobial activity through ion-mediated mechanisms. The pH is a critical factor in tuning particle size, crystallinity, and antimicrobial efficiency.[37]

Overall, the XRD results demonstrate that pH is a crucial parameter in determining the crystallinity, structural quality, and particle formation kinetics of ZnO nanoparticles synthesized *via* green methods. Lower pH (*e.g.*, 2.5) favors slow, controlled crystallization leading to highly crystalline materials, while higher pH (*e.g.*, 10) accelerates nucleation but introduces more defects and structural disorder, as reflected in the broadening and weakening of diffraction peaks.

3.5. Raman and PL results

To further validate the structural properties of the biosynthesized ZnO NPs, Raman spectroscopy was considered (Fig. 6a). The recorded Raman spectra exhibited several

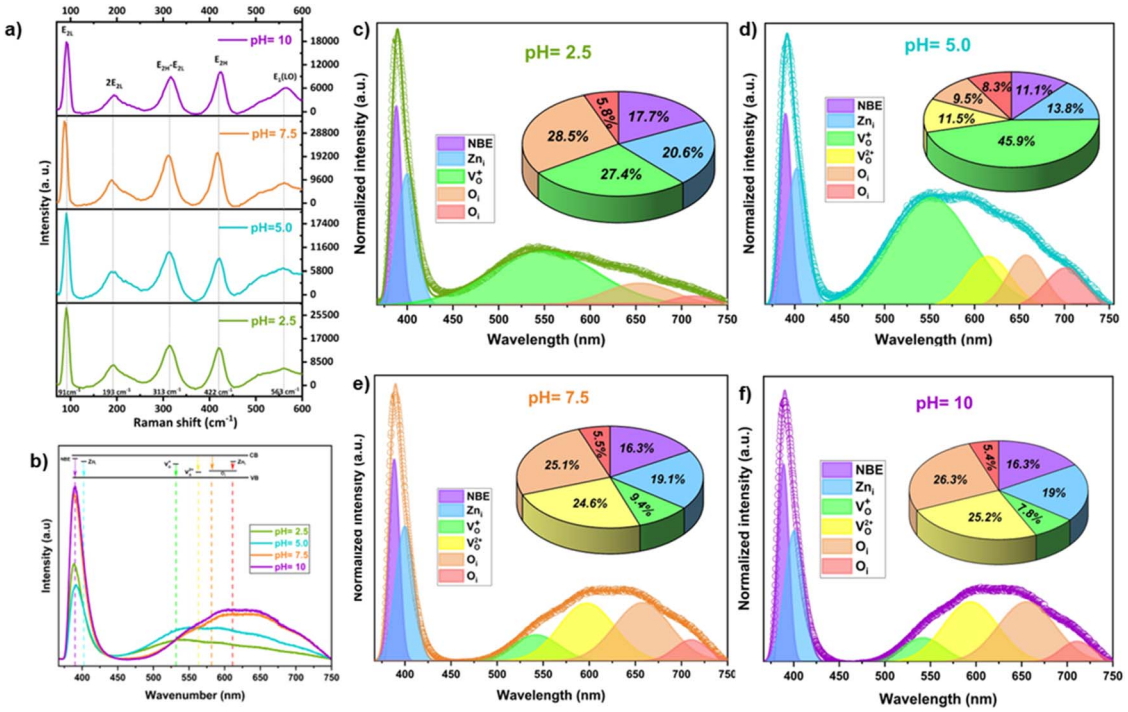

Fig. 6 (a) Raman spectra and (b) PL spectra showing emission regions of ZnO NPs synthesized from *Morinda citrifolia* leaves extract at various pH values. (c–f) Gaussian deconvolution of PL spectra for samples synthesized at (c) pH 2.5, (d) pH 5.0, (e) pH 7.5, and (f) pH 10.0. The deconvolution identifies intrinsic defect states, with the pH 5.0 sample exhibiting the highest concentration of singly ionized oxygen vacancies (V_O^+).

characteristic vibrational modes consistent with the wurtzite ZnO structure, including prominent peaks around 91, 193, 313, 422, and 563 cm^{-1} across all the pH values. The zone-center optical phonons can be classified as $\Gamma = A1 + E_1 + 2E_2 + 2B_1$.[36] The B_1 mode is silent; the A_1 and E_1 modes are both Raman- and infrared-active, while the E_2 mode is only unpolarized Raman-active. The low-frequency mode at ~91 cm^{-1} corresponds to the E_{2L} phonon mode, indicative of Zn sublattice vibrations, while the high-frequency mode at ~422 cm^{-1} is attributed to the E_{2H} mode, associated with oxygen atom vibrations, both of which are Raman active and characteristic of well-crystallized ZnO.

The Raman spectral features correlated well with the XRD results. Samples synthesized at pH 2.5 showed sharp and intense E_{2L} and E_{2H} modes, reflecting high crystallinity and a well-ordered lattice, as also confirmed by the sharp XRD Bragg peaks. In contrast, for the pH 5.0 and 10.0 samples, the intensity of these Raman modes declined, and the peaks became broader, aligning with the observed peak broadening and reduced intensity in the XRD patterns. This behavior indicates increased structural disorder and a higher concentration of lattice imperfections or defects. A particularly significant feature is the E_1(LO) mode at ~563 cm^{-1}, known to be sensitive to oxygen-related defects such as vacancies and interstitials.[38] This peak was most intense in the pH 7.5 sample. Notably, for the pH 10.0 sample, while the E_1(LO) peak remained prominent, its intensity was reduced as compared to pH 7.5 and exhibited significant broadening. This broadening serves as a clear indicator of substantial lattice disorder and strain due to particle aggregation at high pH. This observation is consistent with the PL data, where the pH 10.0 sample exhibited a suppressed green emission indicative of a lower density of singly ionized oxygen vacancies. This is also consistent with the XRD data, where the pH 10 sample exhibited decreased peak intensity and broadening, both indicative of crystalline imperfections. The second-order Raman mode at ~313 cm^{-1}, attributed to the E_{2H}–E_{2L} transition,[29] further supports these findings. Its increased prominence in the samples synthesized at pH 7.5 and 10 implies stronger multi-phonon interactions, often associated with defect-rich structures.

The PL spectra (Fig. 6b) were deconvoluted (Fig. 6c–f) to quantify the contribution of near-band-edge excitonic recombination (NBE) and deep-level emissions (DLE). This sharp and intense UV emission indicates high crystallinity and minimal bulk defects in the ZnO lattice. The blue emission (~400 nm) is typically associated with interstitial zinc (Zn_i). A broad visible emission band from 500 to 700 nm is observed and deconvoluted into several sub-peaks. The visible emission bands are attributed to specific intrinsic defects: green (~530–550 nm) to singly ionized oxygen vacancies (V_O^+), yellow (~580–600 nm) to doubly ionized oxygen vacancies (V_O^{2+}), and orange/red (~650–700 nm) to interstitial oxygen (O_i), consistent with findings by Pathak *et al.*[39] These intrinsic defects are known to facilitate the generation of ROS, which play an important role in the antibacterial and antifungal mechanism of ZnO NPs.[40] The PL spectra were analyzed to relate the observed emissions to potential shifts in bandgap energy and defect density. As shown in Table 3, the NBE emission peaks were centered between 388 nm and 390 nm. The optical bandgap energy (E_g) was calculated using the equation $E_g = 1240/\lambda_{NBE}$. The peak

Table 3 Quantitative analysis of photoluminescence emission characteristics of ZnO NPs

Sample	NBE peak λ_{NBE} (nm)	NBE FWHM (nm)	Optical bandgap E_g (eV)	Vis/NBE ratio	Dominant emission
pH 2.5	388.096	13.473	3.195	3.486	Balanced
pH 5.0	389.754	10.409	3.181	6.775	Green
pH 7.5	388.477	9.439	3.192	3.963	Yellow and orange
pH 10	388.903	9.725	3.188	3.969	Yellow and orange

bandgap of 3.195 eV at pH 2.5 is ascribed to the quantum confinement effect induced by reduced particle size.

Quantitative analysis of the defect density was performed using the Vis/NBE integrated area ratio. The pH 5.0 sample exhibited the highest ratio of 6.775, quantitatively confirming that this sample possesses the highest concentration of optically active defects. At pH 5.0 (Fig. 6d), the PL emission is dominated by a strong green band (~550 nm), attributed to a high concentration of V_O^+, with the visible emission comprising approximately 80% of the total spectrum. This sample is dominated by a massive green emission contribution of 45.9%, corresponding to a high concentration of V_O^+, consistent with findings by Aldeen *et al.*[41] This high density of surface-active V_O^+ defects are critical, as these sites act as electron capture centers that facilitate robust ROS generation. In contrast, samples synthesized at alkaline pH showed a distinct shift in defect type. For the pH 7.5 and pH 10.0 samples (Fig. 6e–f), the green emission (V_O^+) drastically dropped to 9.5% and 7.8%, the Vis/NBE ratio decreased to 3.963 and 3.969. Instead, the spectrum was dominated by deeper defects, with yellow (V_O^{2+}) and orange (O_i) emissions rising to 24.6%, 25.1% and 25.2%, 26.3%, respectively. This quantitative PL data explains the Raman observation: while defects are present, indicated by Raman, they have transitioned from surface-active V_O^+ (at pH 5.0) to deeper, less bioactive V_O^{2+} and O_i defects (at pH 10.0). The sample prepared at pH 2.5 (Fig. 5c) exhibited the highest relative NBE emission (17.7%) among the samples, alongside a balanced distribution of visible defects. This higher NBE contribution corroborates the sharp E_{2H} Raman mode, confirming the superior crystal quality of the pH 2.5 sample.

These findings highlight the critical influence of synthesis pH. The pH 5.0 condition promotes the formation of singly ionized oxygen vacancies (V_O^+), which are the most active sites for antimicrobial mechanisms. At higher pH (7.5 and 10), although lattice disorder persists (broad Raman peaks), the defects evolve into deep-level states (V_O^{2+}/O_i) that are less effective for surface reactivity. Thus, the superior antibacterial potential of the pH 5.0 sample is mechanistically supported by its unique defect composition dominated by V_O^+.

3.6. Antimicrobial mechanism

Mendes *et al.* observed that ZnO NPs synthesized from *Tecoma castanifolia* leaves showed antimicrobial activity by disrupting bacterial ion channels, leading to ionic imbalance and cell death.[42] Similarly, Abebe *et al.* demonstrated that ZnO NPs derived from *Thlaspi arvense* extract acted through electrostatic interactions between their positive surface charge and negatively charged cell wall components in Gram-positive bacteria, causing membrane damage, cytoplasmic leakage, and cell death.[43] Previous studies by Mendes *et al.*[42] and Abebe *et al.*[43] have established that ZnO NPs exert antimicrobial effects through ionic imbalance and electrostatic interactions with bacterial cell walls. Building on this, the antimicrobial mechanism in the present study is proposed to be multifactorial (Fig. 7), driven primarily by ROS generation, Zn^{2+} ion release, and physical interaction, all of which are intrinsically linked to the physicochemical properties modulated by synthesis pH.

Furthermore, cytotoxicity is initiated by physical interaction driven by electrostatic forces. Bacterial cells possess an overall negative charge at physiological pH due to the dissociation of carboxylic groups in the cell wall. Since bacterial surfaces are typically negatively charged, the optimal ZnO NPs synthesized at pH 5.0 facilitate immediate electrostatic attraction due to their positive zeta potential of +9.7 mV, providing a sufficient electrostatic driving force to facilitate immediate attraction to the negatively charged bacterial surfaces. This attraction leads to membrane disruption and subsequent cytoplasmic leakage, as evidenced by the high bactericidal rates. This interaction facilitates cell wall rupture and subsequent penetration, allowing oxidative damage to progress toward the inner cytoplasmic membrane. Consequently, this impairs respiratory activity, causes slow leakage of RNA and proteins, and triggers a rapid efflux of potassium ions (K^+), which is a major factor leading to bacterial inactivation.[44]

The generation of ROS is the central driver, occurring when free electrons (e^-) and holes (h^+) in photoexcited particles interact with aqueous oxygen and water. This process generates superoxide radical anions ($^{\bullet}O_2^-$) *via* the reduction of molecular oxygen ($e^- + O_2 \rightarrow {}^{\bullet}O_2^-$), which subsequently undergoes protonation to form hydrogen peroxide ($2{}^{\bullet}O_2^- + 2H^+ \rightarrow H_2O_2$). Simultaneously, photogenerated holes (h^+) oxidized water molecules (H_2O) or hydroxide ions ($h^+ + H_2O \rightarrow OH^-$) to produce hydroxyl radicals ($h^+ + OH^- \rightarrow {}^{\bullet}OH$), which were highly reactive species playing a significant role in oxidative degradation processes. Crucially, the efficiency of these reactions is dictated by the defect density identified *via* spectroscopic analysis. Specifically, at pH 5.0, PL spectra revealed a dominant green emission (~80%) and the highest Vis/NBE integrated area ratio of 6.8, indicating a high concentration of singly ionized oxygen vacancies (V_O^+). This quantitatively confirms a superior concentration of singly ionized oxygen vacancies compared to other pH levels. These surface defects act as electron capture centers, effectively separating electron–hole pairs and delaying

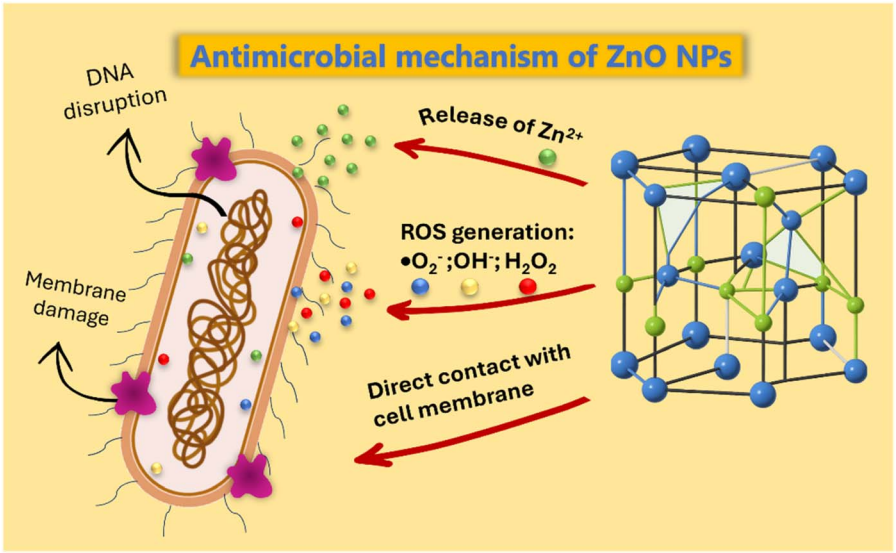

Fig. 7 Antimicrobial mechanism of ZnO NPs.

their recombination, thereby facilitating the robust generation of $^{\bullet}O_2^-$ and $^{\bullet}OH$.

The correlation between high defect density and antimicrobial efficacy observed in our pH 5.0 sample aligns with recent defect engineering strategies for oxide nanomaterials.[17] Our spectroscopic data, interpreted through the lens of recent lattice disorder models,[16] confirms that ionized oxygen vacancies serve as critical electron traps. This mechanism facilitates the generation of ROS, which represents a significant advantage in terms of environmental sustainability by enhancing disinfection efficiency in wastewater applications.[18] By connecting antimicrobial performance with spectroscopic defect analysis, this study provides a framework for designing eco-friendly disinfectants that balance biocidal power with ecological safety.

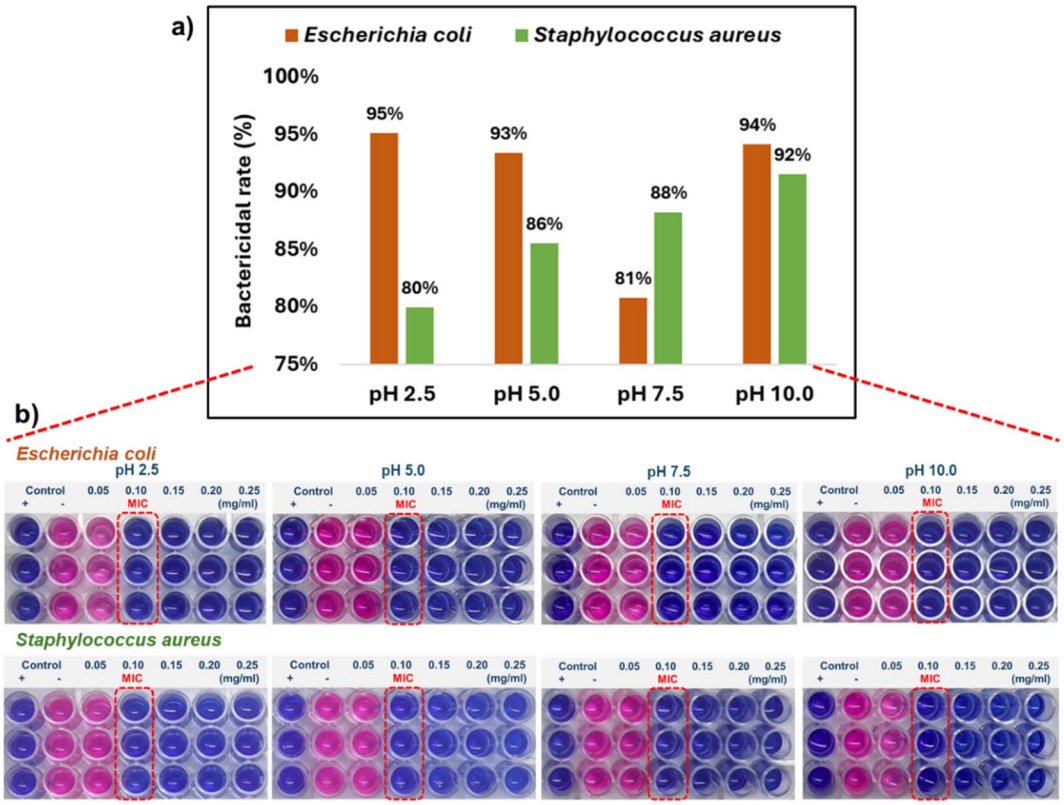

Fig. 8 Antibacterial activity for *Morinda citrifolia* leaves-mediated ZnO NPs with different pH values against *E. coli* and *S. aureus* (a) bactericidal rate (%) at 0.1 mg mL^{-1}; (b) Minimum Inhibitory Concentration (MIC).

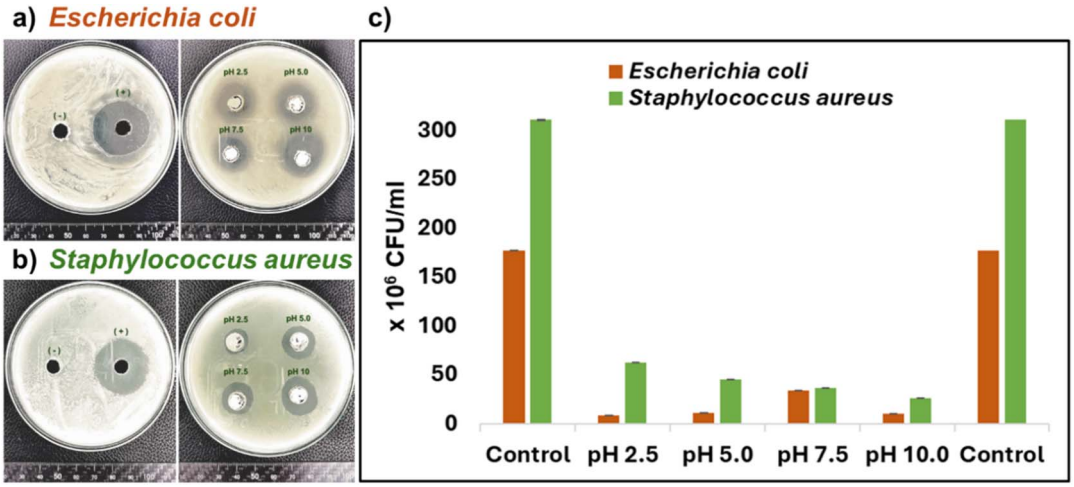

Fig. 9 (a) Antibacterial activity of ZnO NPs on *E. coli* at different pH; (b) antibacterial activity of ZnO NPs on *S. aureus* at different pH; (c) Number of colony-forming units (CFU) of *E. coli* and *S. aureus* after overnight incubation in the presence of ZnO NPs formed at different pH levels.

This high density of V_O^+ explains the superior antimicrobial activity of the pH 5.0 sample, as these ROS induce severe oxidative stress, damaging bacterial membranes, proteins, and DNA. In contrast, the activity of the pH 2.5 sample is governed by the size effect, where the smallest crystallite size and high dispersity maximize the specific surface area. This experimental correlation explains why the pH 5.0 sample achieves high antimicrobial efficacy, comparable even to the pH 2.5 sample, despite its larger particle size. Conversely, at pH 7.5 and pH 10.0, despite observed aggregation, efficacy remained high due to significant lattice disorder indicated by broadened Raman peaks, which sustained ROS production. Additionally, the release of Zn^{2+} ions further destabilizes the bacterial membrane and disrupts enzymatic activity. The internalized NPs promote intracellular aggregation and disrupt cellular homeostasis, ultimately leading to cell death.[45]

The environmental significance of these findings is further elucidated by comparing our defect-engineered ZnO NPs with recent biowaste-derived nanobiocomposites. Mandal *et al.* reported that Ag–Fe_3O_4 nanoparticles incorporated into a collagen matrix exhibited enhanced biocompatibility and thermal stability, offering an eco-friendly strategy for water purification.[18] Similarly, the high antimicrobial potency of our pH 5.0 sample, achieved through spectroscopic defect modulation, ensures effective pathogen inactivation without the need for excessive material loading. This efficiency represents a critical environmental benefit by minimizing the cumulative release of zinc ions into aquatic ecosystems, thereby addressing the risks of secondary pollution while maintaining high disinfection performance in wastewater and biomedical applications.

3.7. Antibacterial performance

The antibacterial activity of *Morinda citrifolia*-mediated ZnO NPs was evaluated against *E. coli* (Gram-negative) and *S. aureus* (Gram-positive) using MIC determination, bactericidal rate assays, and agar well diffusion (Fig. 8 and 9). The Minimum Inhibitory Concentration (MIC) was determined to be 0.10 mg mL^{-1} for both bacterial strains across all synthesis pH levels (2.5, 5.0, 7.5, and 10.0), as evidenced by the visible clarification in the test wells (Fig. 8b). One-way ANOVA analysis Table 4 indicated that the differences in inhibition zone diameters across the various synthesis pH values were statistically significant ($p < 0.05$). Generally, the ZnO NPs exhibited higher efficacy against *E. coli*

Table 4 Analysis of variance of the inhibition zone diameters of ZnO NPs against *E. coli* and *S. aureus*

Source of variation	SS	df	MS	*F*	*P*-Value	F_{crit}
Between groups	5.533	3.000	1.844	6.366	1.63×10^{-2}	4.066
Within groups	2.318	8.000	0.290	One-way ANOVA results for the antibacterial activity of ZnO NPs against *E. coli*		
Total	7.851	11.000				
Between groups	60.856	3.000	20.285	184.105	1.02×10^{-7}	4.066
Within groups	0.881	8.000	0.110	One-way ANOVA results for the antibacterial activity of ZnO NPs against *S. aureus*		
Total	61.737	11.000				

Table 5 Analysis of variance of the inhibition zone diameters of ZnO NPs against *C. albicans*

One-way ANOVA results for the antifungal activity of ZnO NPs against *C. albicans*

Source of variation	SS	df	MS	*F*	*P*-Value	F_{crit}
Between groups	33.862	3.000	11.287	35.524	5.68×10^{-5}	4.066
Within groups	2.542	8.000	0.318			
Total	36.404	11.000				

(bactericidal rates: 95%, 93%, 81%, and 94%) compared to *S. aureus* (80%, 86%, 88%, and 92%). This differential sensitivity is primarily attributed to the distinct cell wall structures. *E. coli* possesses a thin peptidoglycan layer and a lipid-rich outer membrane, making it more susceptible to ROS permeation and membrane disruption. In contrast, *S. aureus* features a thick peptidoglycan layer and lacks an outer membrane, providing a robust barrier that confers higher resistance to nanoparticle penetration.[46] However, the magnitude of this variation between the two strains was found to be dependent on the synthesis pH, which dictates the dominant killing mechanism.

The bactericidal efficiency was significantly modulated by the synthesis pH, showing a direct correlation with the structural defects identified *via* spectroscopy. The sample synthesized at pH 2.5 exhibited the highest bactericidal rate against *E. coli* (95%) and *S. aureus* (80%). This performance was primarily driven by the size effect; as evidenced by SEM and XRD, these particles were smaller and highly dispersed, maximizing the surface contact area with bacterial membranes. The observed ~15% disparity suggests that the size effect dominant at pH 2.5 is more effective against Gram-negative bacteria. While small NPs easily penetrate the outer membrane of *E. coli*, the thick peptidoglycan mesh of *S. aureus* acts as an effective physical sieve, limiting internal accumulation. However, the ZnO NPs synthesized at pH 5.0 demonstrated comparably potent activity (93% against *E. coli*, 86% against *S. aureus*) with significant inhibition zones (17.62 ± 0.72 mm for *E. coli*; 17.05 ± 0.25 mm for *S. aureus*). Crucially, this high efficacy is mechanistically linked to crystallographic defects rather than size alone. As revealed in the PL spectra (Fig. 5d), the pH 5.0 sample exhibited a dominant green emission (~80% of the total spectrum), indicating a high concentration of singly ionized oxygen vacancies (V_O^+). These V_O^+, defects function as electron capture centers, delaying electron–hole recombination and facilitating the robust generation of ROS such as $^{\bullet}O_2^-$ and $^{\bullet}OH$, which induce oxidative stress and lipid peroxidation, leading to

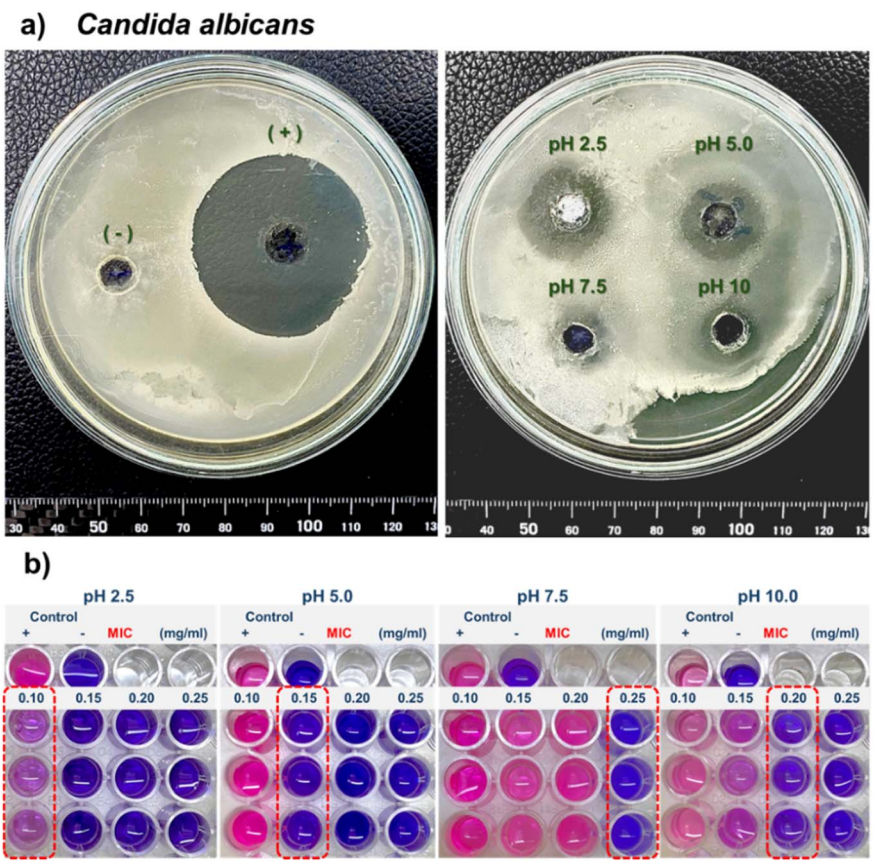

Fig. 10 Antifungal activity of ZnO NPs against *C. albicans* at different pH levels by (a) agar well diffusion at 0.1 mg per mL ZnO NPs and (b) MIC.

bacterial cell death. At this pH, the efficacy gap narrowed (93% *vs.* 86%), indicating that the chemically-driven ROS mechanism is better capable of overcoming the physical barrier of the Gram-positive cell wall than the size-driven mechanism.

In contrast, the pH 7.5 sample showed reduced efficacy due to a larger particle size and lower defect density. Interestingly, despite significant aggregation at pH 10.0 (size ~159 nm), the antibacterial activity remained high (94% for *E. coli*). This apparent anomaly contradicts the conventional size activity relationship but is elucidated by the spectroscopic data. The Raman spectra for the pH 10.0 sample exhibited significant peak broadening and intensity reduction (Fig. 9a), indicative of substantial lattice disorder and a high density of surface imperfections. Unlike surface-active V_O^+ defects at pH 5.0, which primarily promote ROS-mediated attacks, lattice distortion, and structural defects at pH 10.0 facilitate easier dissolution of Zn^{2+} ions from the lattice. Therefore, the enhanced chemical reactivity and Zn^{2+} of the defect-rich surface at higher pH compensate for the loss of geometric surface area caused by aggregation. Remarkably, at pH 10.0, the bactericidal rates for *E. coli* (94%) and *S. aureus* (92%) were nearly identical. This suggests that the high chemical reactivity (ROS and Zn^{2+}) of the defect-rich surfaces compensates for the lack of physical penetration. The released Zn^{2+} ions and ROS can chemically attack the cell wall components regardless of the peptidoglycan thickness, thereby minimizing the variation in activity between Gram-positive and Gram-negative bacteria compared to the physical size effect observed at pH 2.5.

Colony counting assays (Fig. 9c) further confirmed that the pH 5.0 sample achieved a massive reduction in viable bacteria, with *E. coli* decreasing from 177×10^6 CFU mL^{-1} in the control group to only 11.67×10^6 CFU mL^{-1} and *S. aureus* from 311.33×10^6 to 45×10^6 CFU mL^{-1}, corresponding to kill rates of ~93% and ~86%, respectively. This substantiates that the optimization of oxygen vacancies (V_O^+) at pH 5.0 is a critical factor enhancing antibacterial performance, operating synergistically with Zn^{2+} ion release to disrupt cellular integrity.

3.8. Antifungal activity

The antifungal efficacy of ZnO NPs against *Candida albicans* exhibited a distinct dependence on synthesis pH. As shown in Table 5, the synthesis pH significantly influenced the antifungal activity, with statistically significant differences observed among the pH groups ($p < 0.05$). Based on the quantitative inhibitory metrics (MIC and inhibition zone), the sample synthesized at pH 2.5 represented the optimal antifungal condition. As shown in Fig. 10, the pH 2.5 sample achieved the lowest MIC (0.10 mg mL^{-1}) and the largest inhibition zone (15.47 ± 0.28 mm), significantly outperforming the pH 7.5 (MIC = 0.25 mg mL^{-1}; zone = 11.14 ± 0.33 mm) and pH 10.0 (MIC = 0.20 mg mL^{-1}; zone = 11.74 ± 0.24 mm) samples. This superior potency is primarily attributed to the size effect, as the pH 2.5 sample possessed the smallest crystallite size and highest dispersity, maximizing the specific surface area for interaction with the fungal cell wall.

However, the sample synthesized at pH 5.0 also demonstrated remarkably strong antifungal activity (MIC = 0.15 mg mL^{-1}; zone = 13.39 ± 1.01 mm), which provides critical insight into the defect-mediated mechanism. Unlike the size-driven activity at pH 2.5, the efficacy at pH 5.0 is mechanistically correlated with the highest defect density. This mirrors the dominant green emission (~80%) observed in the PL spectra, identifying a high concentration of singly ionized oxygen vacancies (V_O^+). These defects act as catalytic centers for ROS generation and Zn^{2+} release, creating oxidative stress potent enough to disrupt the eukaryotic membrane of *C. albicans*. Therefore, while pH 2.5 is optimal for maximizing bactericidal rates *via* size reduction, pH 5.0 highlights the pivotal role of crystal defects in enhancing biological reactivity.

4. Conclusion

ZnO nanoparticles were successfully synthesized *via* a green hydrothermal method using *Morinda citrifolia* leaf extract, with their physicochemical properties significantly modulated by the synthesis pH (2.5 to 10.0). Characterization *via* SEM and XRD confirmed the formation of pure hexagonal wurtzite ZnO with nearly spherical nanoparticles forming dense, agglomerated clusters and high crystalline integrity. The core contribution of this research is the discovery that antimicrobial potency is governed more by specific defect types than by particle size alone. While the pH 2.5 sample excelled due to the physical size effect, quantitative PL deconvolution revealed that pH 5.0 optimizes the concentration of singly ionized oxygen vacancies (V_O^+), which account for ~80% of the visible emission and act as primary catalytic centers for ROS generation. These defect-rich states correlated with superior broad-spectrum antimicrobial performance ($Gram^+$/$Gram^-$/fungi), with inhibition zones at 100 mg mL^{-1} reaching 17.053 mm (*S. aureus*), 17.617 mm (*E. coli*), and 13.39 mm (*C. albicans*). Furthermore, the pH 5.0 and pH 10.0 samples demonstrated that lattice disorder and surface-active defects, evidenced by the Raman E_1(LO) mode and green emission ratios, can effectively compensate for increased particle size, maintaining high bactericidal rates (~93% and 94% against *E. coli*). The statistically significant correlation between spectroscopic data and microbial inhibition zones confirms that pH-controlled defect engineering is a viable strategy for enhancing the reactivity of biogenic ZnO. These findings underscore the role of plant phytochemicals in tailoring the bio-interface of nanomaterials and provide a predictive model for developing targeted biomedical applications. To further improve synthesis efficiency and preserve thermolabile phytochemicals, future studies should optimize extraction protocols, such as utilizing lower drying temperatures (40–60 °C) or lyophilization. Future evaluation against clinical isolates and multidrug-resistant strains will further validate their therapeutic potential.

Author contributions

Tien Cam Thi Nguyen: writing – original draft, formal analysis, data curation, investigation. Phuc My Thi Truong: investigation,

data curation. Ly Ngoc Thi Le: investigation, data curation. Uyen Tu Thi Doan: methodology, data curation. Khanh Duy Nguyen: methodology, data curation. Ngoc Kim Pham: methodology, data curation. Vinh Cao Tran: methodology, validation. Lan My Thi Nguyen: methodology, data curation, validation. Anh Tuan Thanh Pham: conceptualization, resources, methodology, writing – review & editing, supervision.

Conflicts of interest

The authors declare that there are no conflicts of interest.

Data availability

The datasets supporting the findings of this article are available within the main text and supplementary information (SI). Supplementary information is available. See DOI: https://doi.org/10.1039/d6ra00644b.

Acknowledgements

This research is funded by University of Science, VNU-HCM under grant number T2024-160.

References

1 J. Burgos, G. Gómez, A. M. Leiva and G. Vidal, *J. Water Process Eng.*, 2025, **70**, 106966.
2 S. Jia, C. Qi, S. Xu, L. Yang and Q. Sun, *J. Mater. Sci. Technol.*, 2025, **225**, 212–226.
3 M. Kumar, S. Mahmood, S. Chopra and A. Bhatia, *Int. J. Biol. Macromol.*, 2024, **267**, 131335.
4 B. Qu, Z. Xiao and Y. Luo, *J. Agric. Food Res.*, 2025, **19**, 101743.
5 A. K. Khajuria, A. Kandwal, R. K. Sharma, R. K. Bachheti, L. A. Worku and A. Bachheti, *Sci. Rep.*, 2025, **15**, 6541.
6 J. Zhu, T. Wen, Y. Ma, Q. Zeng, Y. Lin, Y. Liu, S. Chen, Q. Wang and W. Zhou, *Adv. Healthcare Mater.*, 2025, **14**, 2501009.
7 Z. Guo, H. Chen, R. Hu, J. Wang, M. Wu, Y. Wu, T. Qiang, H. Mou, X. Du, S. Guo and X. Zhou, *Sci. Rep.*, 2025, **15**, 26780.
8 N. A. Hussien, M. A. E. F. Khalil, M. Schagerl and S. S. Ali, *Int. J. Nanomed.*, 2025, **20**, 4299–4317.
9 Y. Vinayagam, G. Venkatraman and V. D. Rajeswari, *Int. Biodeterior. Biodegrad.*, 2025, **200**, 106036.
10 S. Dhiman, A. Kumari, S. Kumari and R. Sharma, *J. Environ. Chem. Eng.*, 2025, **13**, 116296.
11 A. I. Al-Tameemi, M. J. Masarudin, R. A. Rahim, R. Mizzi, V. J. Timms, N. M. Isa and B. A. Neilan, *Appl. Microbiol. Biotechnol.*, 2025, **109**, 32.
12 D. N. Mishra, L. Prasad and U. Suyal, *Front. Microbiol.*, 2025, **16**, 1506695.
13 W. A. Abo-Shanab, S. E. Elsilk, S. S. Afifi and R. A. El-Shenody, *J. Soil Sci. Plant Nutr.*, 2025, **25**, 2742–2762.
14 A. Mohammadi, N. Hashemi, M. Ghassabzadeh, A. Sharafi, A. Yazdinezhad and H. Danafar, *Sci. Rep.*, 2025, **15**, 20853.
15 N. Shreyash, S. Bajpai, M. A. Khan, Y. Vijay, S. K. Tiwary and M. Sonker, *ACS Appl. Nano Mater.*, 2021, **4**, 11428–11457.
16 A. Murugan, P. Arumugam, S. Vajiravelu and A. Mandal, *J. Mol. Struct.*, 2025, **1321**, 139710.
17 A. Mandal, A. Poongan, E. Dhineshkumar and E. Murugan, *ACS Appl. Eng. Mater.*, 2023, **1**, 2137–2152.
18 A. Mandal, E. Dhineshkumar and T. P. Sastry, *Clean Technol. Environ. Policy*, 2023, **25**, 3285–3302.
19 C. Hu, W. Zhu, Y. Lu, Y. Ren, J. Gu, Y. Song and J. He, *Environ. Sci. Pollut. Res.*, 2023, **30**, 28818–28829.
20 M. Aisha, A. Kalid and A. O. John, *Int. J. Integr. Educ.*, 2020, **3**, 112–116.
21 R. M. Jebir and Y. F. Mustafa, *Eurasian Chem. Commun.*, 2022, **4**, 736–744.
22 M. Shoge, O. J. Ogunbiyi and K. M. Muhammad, *J. Ethnopharmacol. Toxicol.*, 2025, **3**, 1–9.
23 M. Priya, R. Venkatesan, S. Deepa, S. S. Sana, S. Arumugam, A. M. Karami, A. A. Vetcher and S. Kim, *Sci. Rep.*, 2023, **13**, 18838.
24 J. Sukumaran, R. Venkatesan, M. Priya and S. Kim, *Inorg. Chem. Commun.*, 2024, **170**, 113411.
25 A. H. Labulo, O. A. David and A. D. Terna, *Chem. Pap.*, 2022, **76**, 7313–7325.
26 M. Nagalingam, S. Rajeshkumar, S. K. Balu, M. Tharani and K. Arunachalam, *J. Nanomater.*, 2022, **2022**, 2155772.
27 N. Senthilkumar, E. Nandhakumar, P. Priya, D. Soni, M. Vimalan and I. V. Potheher, *New J. Chem.*, 2017, **41**, 10347–10356.
28 M. Arellano-Cortaza, E. Ramírez-Morales, U. Pal, G. Pérez-Hernández and L. Rojas-Blanco, *Ceram. Int.*, 2021, **47**, 27469–27478.
29 P. Sathish, N. Dineshbabu, K. Ravichandran, T. Arun, P. Karuppasamy, M. SenthilPandian and P. Ramasamy, *Ceram. Int.*, 2021, **47**, 27934–27941.
30 A. F. Abdulrahman, S. M. Ahmed, S. M. Hamad, M. A. Almessiere, N. M. Ahmed and S. M. Sajadi, *Chin. J. Phys.*, 2025, **71**, 175–189.
31 M. Priya, R. Venkatesan, S. Deepa, S. S. Sana, S. Arumugam, A. M. Karami, A. A. Vetcher and S. Kim, *Sci. Rep.*, 2023, **13**, 18838.
32 M. Y. Al-Darwesh, S. S. Ibrahim and L. L. Hamid, *Nano-Struct. Nano-Objects*, 2024, **38**, 101163.
33 A. G. Zewudie, E. A. Zereffa, T. A. Segne, H. C. A. Murthy, C. R. Ravikumar, D. Muniswamy and B. B. Binagdie, *Rev. Adv. Mater. Sci.*, 2023, **62**, 20220307.
34 M. MuthuKathija, M. S. M. Badhusha and V. Rama, *Appl. Surf. Sci. Adv.*, 2023, **15**, 100400.
35 S. Raha and M. Ahmaruzzaman, *Nanoscale Adv.*, 2022, **4**, 1868–1925.
36 T. U. D. Thi, T. T. Nguyen, Y. D. Thi, K. H. T. Thi, B. T. Phan and K. N. Pham, *RSC Adv.*, 2020, **10**, 23899–23907.
37 T. Vitasovic, G. Caniglia, N. Eghtesadi, M. Ceccato, E. D. Bøjesen, U. Gosewinkel, G. Neusser, U. Rupp, P. Walther, C. Kranz and E. E. Ferapontova, *ACS Appl. Mater. Interfaces*, 2024, **16**, 30847–30859.
38 C. Kalyani, I. V. S. Reddy, P. Raju and P. M. S. Raju, *Ceram. Int.*, 2025, **51**, 17007–17014.
39 J. Pathak, S. B. Akhani and M. S. Rathore, *Mater. Today: Proc.*, 2024, DOI: 10.1016/j.matpr.2024.01.004, In press.

40 M. S. Rathore, H. Verma, S. B. Akhani, J. Pathak, U. Joshi, A. Joshi, C. Prakash, K. Kaur and A. Oza, *Mater. Adv.*, 2024, **5**, 3472–3481.
41 T. S. Aldeen, H. E. A. Mohamed and M. Maaza, *J. Phys. Chem. Solids*, 2022, **160**, 110313.
42 C. R. Mendes, G. Dilarri, C. F. Forsan, V. Sapata, P. R. M. Lopes, P. Moraes, R. N. Montagnolli, H. Ferreira and E. D. Bidoia, *Sci. Rep.*, 2022, **12**, 2658.
43 B. Abebe, E. A. Zereffa, A. Tadesse and H. C. A. Murthy, *Nanoscale Res. Lett.*, 2020, **15**, 190.
44 N. A. A. Yusof, N. M. Zain and N. Pauzi, *Int. J. Biol. Macromol.*, 2019, **124**, 1132–1136.
45 S. Sasi, P. H. F. Fasna, T. K. B. Sharmila, C. S. Julie Chandra, J. V. Antony, V. Raman, A. B. Nair and H. N. Ramanathan, *J. Alloys Compd.*, 2022, **924**, 166431.
46 G. Guan, L. Zhang, J. Zhu, H. Wu, W. Li and Q. Sun, *J. Hazard. Mater.*, 2021, **402**, 123542.